PCCP

Accepted Manuscript

Volume 1 | Number 1 | Jan 2013 | Pages 1–100

PCCP

Physical Chemistry Chemical Physics
www.rsc.org/pccp

ROYAL SOCIETY OF CHEMISTRY

This is an *Accepted Manuscript*, which has been through the Royal Society of Chemistry peer review process and has been accepted for publication.

Accepted Manuscripts are published online shortly after acceptance, before technical editing, formatting and proof reading. Using this free service, authors can make their results available to the community, in citable form, before we publish the edited article. We will replace this *Accepted Manuscript* with the edited and formatted *Advance Article* as soon as it is available.

You can find more information about *Accepted Manuscripts* in the **Information for Authors**.

Please note that technical editing may introduce minor changes to the text and/or graphics, which may alter content. The journal's standard **Terms & Conditions** and the **Ethical guidelines** still apply. In no event shall the Royal Society of Chemistry be held responsible for any errors or omissions in this *Accepted Manuscript* or any consequences arising from the use of any information it contains.

ROYAL SOCIETY OF CHEMISTRY

www.rsc.org/pccp

Physical Chemistry Chemical Physics

RSCPublishing

ARTICLE

ReaxFF Molecular Dynamics Simulations on Lithiated Sulfur Cathode Materials[†]

Md Mahbubul Islam[a], Alireza Ostadhossein[b], Oleg Borodin[c], A. Todd Yeates[d], William W. Tipton[e], Richard G. Hennig[e], Nitin Kumar[f], and Adri C. T. van Duin[a*]

Sulfur is a very promising cathode material for the rechargeable energy storage devices. However, sulfur cathodes undergo a noticeable volume variation upon cycling, which induces mechanical stress. In spite of intensive investigation of the electrochemical behavior of the lithiated sulfur compounds, their mechanical properties are not very well understood. In order to fill this gap, we developed a ReaxFF interatomic potential to describe Li-S interactions and performed molecular dynamics (MD) simulations to study the structural, mechanical, and kinetic behavior of the amorphous lithiated sulfur (a-Li$_x$S) compounds. We examined the effect of lithiation on material properties such as ultimate strength, yield strength, and Young's modulus. Our results suggest that with increasing lithium content, the strength of lithiated sulfur compounds improves, although this increment is not linear with lithiation. The diffusion coefficients of both lithium and sulfur were computed for the a-Li$_x$S system at various stages of Li-loading. A grand canonical Monte Carlo (GCMC) scheme was used to calculate the open circuit voltage profile during cell discharge. The Li-S binary phase diagram was constructed using genetic algorithm based tools. Overall, these simulation results provide insight into the behavior of sulfur based cathode materials that are needed for developing lithium-sulfur batteries.

1. Introduction

Over the last two decades, lithium-ion batteries (LIBs) have become ubiquitous in portable consumer electronics. However, the limited capacities of LIBs impede their application in electric vehicles (EVs) and smart-grids.[1,2] Automotive applications require significant improvements in the capacity of electrode materials to allow long trips (i.e. >300km) in a single charging. [3,4] Sulfur based cathode materials for Li-S batteries are considered a very promising alternative to the conventional transition metal oxide/phosphate cathodes[5] due to their high capacity, energy density, non-toxicity, and natural abundance[6]. The theoretical specific capacity of sulfur is 1672 mAhg^{-1}, which is 10 times higher than that of commonly-used LiCoO$_2$ cathodes, and it has a theoretical specific energy density of 2600 Whkg^{-1}, assuming complete reaction to Li$_2$S.[3,6,7]

In current battery technologies, the capacity of the cathodes is substantially lower than that of commercially available anode materials, such as graphite. Moreover, high capacity Si and Sn based anodes are being developed.[8–12] These materials have theoretical specific capacities of 4200 mAhg^{-1} and 900 mAhg^{-1}, respectively.[13] However, any breakthrough in the capacity of the anode materials must be accompanied by improvements to the cathode to develop high-performance batteries to meet next generation energy demand.

Although sulfur exhibits great promise, commercialization of Li-S batteries has been thwarted by several complex problems, such as significant structural and volume changes of the cathode, the high reactivity of lithium, dissolution of intermediate polysulfides into the electrolytes, poor electronic and ionic conductivities of sulfur and Li$_2$S, and safety concerns.[14–18] Volume expansion of the sulfur composite cathode occurs during discharging (lithium intercalation) and contraction during charging (lithium de-intercalation).[19] This active material breathing induces stress in the cathode material, and the active material loses its electrical contact with the conductive substrate or with the current collector.[20] Numerous approaches have been reported in the literature to accommodate volume changes, including sulfur-coated multi-walled carbon nanotubes composite material,[21,22] graphene wrapped sulfur particles,[23] and reduced graphene oxide encapsulated sulfur.[24] These approaches demonstrate high initial capacity, but rapid capacity fading due to cathode degradation still greatly limits performance.

Furthermore, a great deal of recent studies of Li-S batteries used elemental lithium as anode material.[14,20,25–27] The lithium anode yields high capacity, but it has low cycling efficiency and forms lithium dendrites on the anode surface during cycling that can penetrate the separator leading to short circuit.[25,28] To inhibit dendrite formation, Li-ion conducting passivation layers using Li$_3$N,[29] Li$_2$CO$_3$,[30] and LiPON,[31] have been suggested. These protective thin films suppress lithium dendrite formation, but a high cost of fabrication has limited their use.[32] Lithium dendrite formation issues have not yet been fully resolved, restricting the use of Li-metal anodes in commercial batteries.[33] Recently, lithium-metal free batteries that use silicon or tin instead of elemental lithium in the anode have received much attention due to improved safety properties.[34] In these systems, neither the sulfur cathode nor the Si or

Sn anode contains lithium originally, so either the cathode or the anode must be prelithiated to provide a lithium source. To this end, systems composed of Li_2S cathodes and Si anodes have been studied by several previous authors.[16,35,36] However, relatively low lithium diffusivity and high electronic resistivity cause a large potential barrier to activate the Li_2S cathode.[35] He and coworkers[37] investigated a prelithiated sulfur composite/graphite lithium ion cell, which was fabricated using electrochemical lithiation. Li-ion diffusivity in lithiated sulfur depends on the lithium concentration, and lithiated cathode materials possess lower specific capacity than their non-lithiated counterparts.[38]

While significant progress towards improving performance of the Li-S battery has been achieved[17], there is a lack of understanding of mechanical and structural properties of the lithiated sulfur compounds. Molecular dynamics (MD) simulations are well suited for examination of the a-Li_xS as a function of lithiation provided an accurate representation of the intermolecular interactions and chemical reactions is achieved. Such simulations are expected to provide fundamental understanding of the material properties such as understanding the morphological changes a-Li_xS undergoes, and the mechanical degradation of this electrode material at the atomistic level. To the best of our knowledge, no MD simulations have been performed on a-Li_xS systems, probably due to lack of an accurate intermolecular potential. Previously[39], we reported electrolyte chemistry and an *ex-situ* anode surface treatment process for Li-S batteries. In this study, we describe the development of a Li-S ReaxFF potential to model Li-S interactions and use it to investigate the structural evolution, mechanical properties, and diffusion characteristics of a-Li_xS systems.

2. ReaxFF background

ReaxFF is a general bond order[40,41] (BO) based empirical force field method which allows bond breaking and formation during simulations. The general form of the ReaxFF energy terms are shown below

$$E_{system} = E_{bond} + E_{over} + E_{under} + E_{lp} + E_{val} + E_{tor} + E_{vdWaals} + E_{Coulomb}$$

where partial energy contributions include bond, over-coordination penalty and under-coordination stability, lone pair, valence, and torsion, non-bonded interactions van der Waals, and Coulomb energies, respectively.

ReaxFF uses the concept of bond orders to determine the bonded interactions among all the atoms in a system. BOs are continuous function of distance between bonded atoms and contributions from sigma, pi, and double-pi bonds are calculated from the following expression.

$$BO'_{ij} = BO_{ij}{}^{\sigma} + BO_{ij}{}^{\pi} + BO_{ij}{}^{\pi\pi}$$
$$= exp\left[p_{bo1}\cdot\left(\frac{r_{ij}}{r_o{}^{\sigma}}\right)^{p_{bo2}}\right]$$
$$+ exp\left[p_{bo3}\cdot\left(\frac{r_{ij}}{r_o{}^{\pi}}\right)^{p_{bo4}}\right]$$
$$+ exp\left[p_{bo5}\cdot\left(\frac{r_{ij}}{r_o{}^{\pi\pi}}\right)^{p_{bo6}}\right]$$

where $BO_{ij}{}^{\sigma}$, $BO_{ij}{}^{\pi}$, and $BO_{ij}{}^{\pi\pi}$ are the partial contributions of σ, π- and double π-bonds between atoms i and j, r_{ij} is the distance

between i and j, $r_o{}^{\sigma}$, $r_o{}^{\pi}$, and $r_o{}^{\pi\pi}$ are the bond radii of σ, π- and double π-bonds, respectively, and p_{bo} terms are empirical parameters fit to experimental or quantum data.

All of the connectivity dependent interactions, i.e. the valence and torsion energy, are contingent on BO. Hence their energy contribution diminishes upon bond breaking. Non-bonded interactions, i.e. the van der Waals and Coulomb, are calculated between every pair of atoms, regardless of their connectivity. Excessive repulsion at short distances is prevented by adding a shielding parameter in non-bonded energy expressions.[42] Utilization of a seventh order taper function in the non-bonded interaction energies eliminates any energy discontinuity.[43] This treatment of nonbonded interactions enables ReaxFF to describe covalent, ionic, and intermediate materials, and thus enhances its transferability.[44] ReaxFF uses a geometry-dependent charge calculation scheme, the Electronegativity Equalization Method (EEM)[45] for charge calculation. For a more detailed description of the ReaxFF method, see van Duin *et al.*,[46] Chenoweth *et al.*,[47] and Russo Jr. *et al.*.[48]

3. Force Field Development

Development of our ReaxFF force field for the Li-S system was initiated by merging previously published lithium[49] and sulfur[50] parameters. In the fitting procedure, these parameters were extensively trained against quantum mechanics (QM) data describing bond dissociation, angle distortion, equation of state, and heats of formation of crystalline phases and molecules. The optimization of the parameters was performed via a successive one-parameter search technique[51] to minimize the sum of following error

$$Error = \sum_i^n \left[\frac{(x_{i,QM} - x_{i,ReaxFF})}{\sigma_i}\right]^2$$

where x_{QM} is the QM value, x_{ReaxFF} is the ReaxFF calculated value, and σ_i is the weight assigned to data point, i.

Non-periodic QM calculations used in this study were performed in the GAMESS[52] program using second-order Møller–Plesset (MP2)[53] method in conjunction with aug-cc-pVTZ basis set.

To parameterize the ReaxFF bond energy data, we carried out QM calculations for the Li-S and S-S bond dissociation in various molecules, such as, Li_2S_2, and LiSH. Figure 1a-c compares ReaxFF and QM results for the bond dissociation. In each case, we constructed ground state geometries through full geometry optimization. In order to obtain dissociation profiles, bond restraint was applied in the atom pair of interest while rest of the structure was allowed to relax during minimization. Bond distances between Li and S were varied from 1.5Å to 6.0 Å. The equilibrium bond lengths predicted by the QM and ReaxFF are 2.04 and 2.2Å, respectively. The ReaxFF calculated Li-S equilibrium bond length is closer to the Boldyrev et al.[54] reported value of 2.15Å. It can be seen that in the QM energy profile the lowest energy state switches from singlet to triplet at Li-S bond stretching beyond 3.5A, and ReaxFF nicely captures this phenomenon by reproducing the lowest energy states. In the S-S bond dissociation energy profile of Li_2S_2, the QM energy for the singlet manifold is the Spin Component Scaled (SCS) MP2, which is claimed to be more accurate for bond breaking. Likewise, the Li-S bond energy profile, in S-S bond stretching, ReaxFF predicts the ground state that corresponds to the singlet state of the QM energy landscape. ReaxFF calculated S-S bond length in
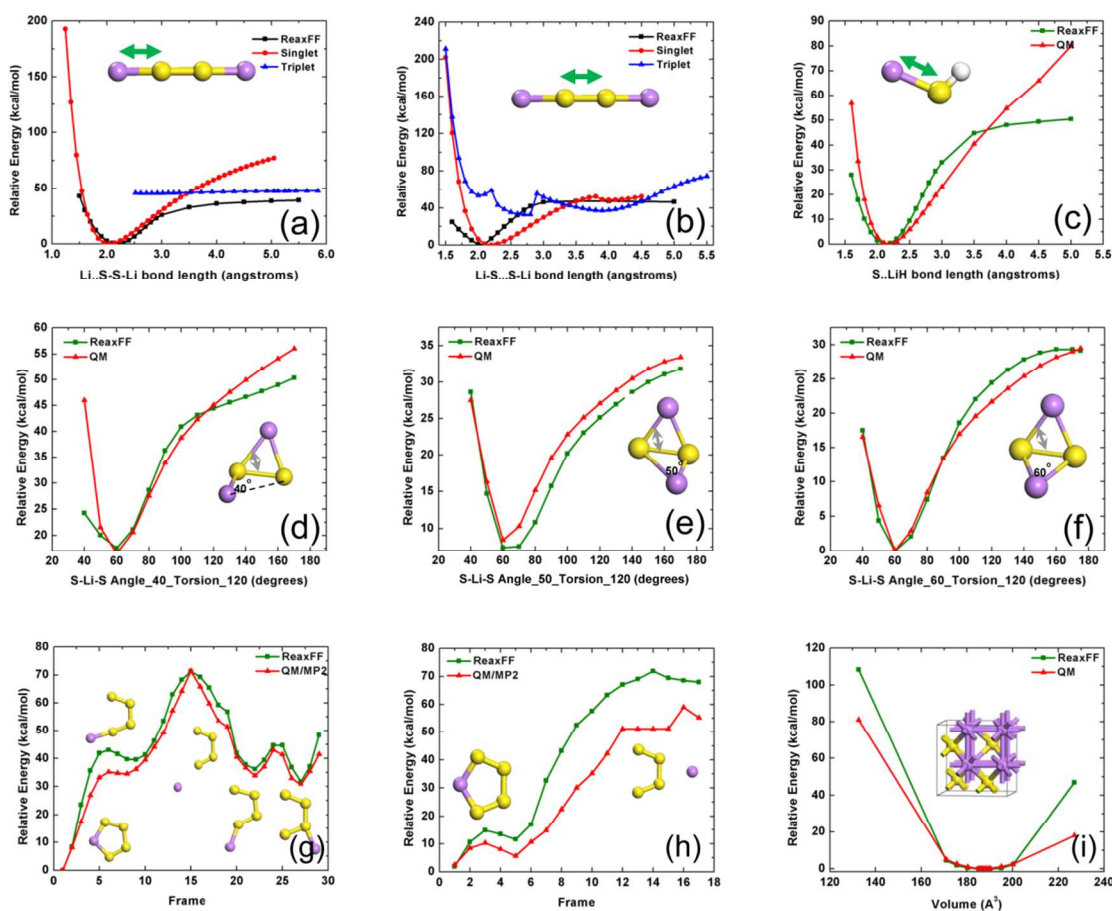
Figure 1. QM and ReaxFF data: bond dissociation curves for (a) Li-S bond in Li_2S_2, (b) S-S bond in Li_2S_2, (c) S-Li bond in LiSH, S-Li-S valence angle distortion in Li_2S_2 keeping S-Li-S angle at (d) 40º (e) 60º (f) 80º (g) Equation of state for Li_2S crystal structure (h) for the migration of a Li-cation around an S_4-anion, and (i) for the dissociation of a Li-cation from an S_4-anion. Yellow and purple represent sulfur and lithium atom, respectively. QM=MP2/aug-cc-pVTZ for (a-h) and GGA/PBE for (i)

D_{4d} cyclic S_8 is 2.17A, which is consistent with the value of 2.08A from the gas phase cluster calculations by Wong *et al.*[55] The ReaxFF dissociation energy for both Li-S and S-S bonds are within 5 kcal/mol of the QM results. Good agreement between ReaxFF and QM are also achieved for Li-S bond dissociation in the LiSH molecule.

In order to optimize S-Li-S and S-S-Li valence angle parameters, we performed QM calculations for these valence angles on Li_2S_2 molecule at a fixed torsion angle. In each case, we kept the S-Li-S angle fixed at a value, while the S-S-Li angle was varied from 40º to 170º to get the energy response for the angle bending. For fitting, we calculated ReaxFF energies of each of the valence angle configurations. These are shown along with corresponding QM energies in Figures 1d-f, and we see that ReaxFF correctly reproduces QM equilibrium angles and the overall energy profile.

An equation of state calculation was performed on crystalline Li_2S (space group no. 225). We carried out periodic QM calculation based on density-functional theory (DFT).[56,57] The Vienna *ab initio* simulation package (VASP) was used to solve the Kohn-Sham equations with periodic boundary conditions and a plane-wave basis set.[58,59] We employed Blöchl's all-electron frozen core projector augmented wave (PAW) method[60] and electron exchange and correlation is treated within the generalized gradient approximation

(GGA) of PBE.[61] The energy cutoff on the wave function is taken as 600 eV and the Monkhorst-Pack scheme was used for the k-point sampling with 5x5x5 k-point grid. We applied compression and expansion with respect to the equilibrium volume of the crystal to calculate QM energies at different volume state. Next, during force field optimization, energies calculated from the ReaxFF corresponding to each volume are compared with the QM data. Figure 1i shows the EOS of the Li_2S crystal as predicted by ReaxFF and QM. We see that ReaxFF acceptably reproduces the QM results near the equilibrium. ReaxFF predicts the lattice constant of Li_2S crystal as 5.75A, which is within 0.5% of the reported experimental value of 5.72A.[62]

Furthermore, we trained our force field for an Li cation migration around and dissociation from an S_4 anion. Geometry of S_4^{2-} was fixed. ReaxFF parameters were fitted against the MP2/aug-cc-pVTZ level of QM results, and the data in Figure 1g and Figure 1h were obtained. We see good agreement of the ReaxFF and QM results for the Li-migration pathway (Figure 1g) and ReaxFF reasonably reproduces QM energetics for Li-dissociation (Figure 1h).

Heats of formation (HF) of various crystalline and gas phase lithium-sulfur species were also utilized in force field fitting. Heats of formation of Li_xS species were calculated with respect to S_8 molecule and bcc-Li were calculated using following relation

$$\Delta E = E_{Li_xS} - xE_{Li} - E_S$$

where E_{LixS} is the total energy of the Li-S system, x is the atomic fraction of lithium, and E_{Li} and E_S are the energies per atom of bcc-Li and sulfur, respectively. Data obtained from the ReaxFF and QM methods are presented in Table 1. The results in Table 1 indicate that ReaxFF reasonably reproduces the HF of the Li_xS species studied.

Table 1: Heats of formation of different Li_xS crystals and molecules as calculated from the ReaxFF and QM (MP2/aug-cc-pVTZ)

Species	ReaxFF(eV)	QM (eV))
Li_2S crystal	-3.88	-4.47
LiS crystal	-1.96	-1.89
LiS_6	-0.79	-0.75
LiS_7	-0.05	-0.67
LiS_8	-0.18	-0.74
LiS	0.95	1.37
LiS_3	-0.74	-0.65
Li_2S	-0.22	-0.59

Reaction energies of various polysulfides, Li_xS_y were calculated and ReaxFF energies are compared with the QM results reported by Assary *et al.*[63] and represented in Table 2. QM calculations were performed using coupled cluster based highly accurate G4MP2[64] with B3LYP/6-31G(2df,p) level of theory. ReaxFF qualitatively reproduces the QM reaction energies of the major polysulfides involved in Li-S battery operation. However, some of the values, e.g. reaction 3 in the Table 2 differ from the corresponding QM data. These reaction pathways were not contained in the training set, and as such there are some deviations between ReaxFF and DFT, however, ReaxFF reproduces the trends in these gas phase reaction energies, which is important to describe the condensed phase simulations considered in this study. In these calculations, Li_2 and cyclic S_8 were used as reference value.

Table 2: Comparison of the reaction energies of various polysulfides as calculated using ReaxFF and G4MP2 level of theory[63]

Reactions	ΔE(eV):ReaxFF	ΔE(eV):QM[63]
$S_8 + 2Li \rightarrow Li_2S_8$	-5.61	-6.02
$Li_2S_8 \rightarrow Li_2S_5 + S_3$	1.51	1.11
$Li_2S_8 \rightarrow Li_2S_4 + (1/2)S_8$	0.59	0.18
$Li_2S_4 \rightarrow Li_2S_2 + (1/4)S_8$	1.03	1.14
$2Li_2S_4 \rightarrow 2Li_2S_3 + (1/4)S_8$	1.35	0.96
$2Li_2S_3 \rightarrow 2Li_2S_2 + (1/4)S_8$	0.72	1.32
$2Li_2S_2 \rightarrow 2Li_2S + (1/4)S_8$	3.61	2.10
$Li_2S_8 \rightarrow LiS_6 + LiS_2$	1.81	2.36

Overall, ReaxFF energy descriptions are in good agreement with the QM data, which establishes the capability of the force field to describe the chemistry of lithium sulfur interactions. Force field parameters are given in the supporting information.

4. Simulation methodology

We employed our Li-S force field to study various lithiated sulfur configurations, Li_xS (x = 0.4, 0.8, 1, 1.2, 1.6, 2.0). Initial geometries were constructed by randomly dispersing lithium atoms at the given ratios in an α-sulfur phase comprised of 2048 atoms. Lithiated sulfur geometries were relaxed using a conjugate gradient minimization scheme. We created amorphous structures by slowly heating the initial structures to 1600K and then rapidly quenching them to 300K. Temperature and pressure were regulated using the Berendsen thermostat and barostat[65], respectively. To obtain the room temperature densities of these annealed structures, NPT (constant pressure, temperature) simulations were performed at 300K and atmospheric pressure. The temperature and pressure damping constants used in both annealing and the NPT simulations were 100fs and 2500fs, respectively. Next, final structures from the 300K NPT simulations were taken from each of the given configurations, and NVT (constant volume, temperature) simulations were performed at various temperatures (i.e. 300K, 600K, 800K, 1000K, 1200K, and 1600K). Temperature and pressure damping constants were 500 and 5000 fs, respectively, and the simulation duration was about 1 ns. High temperature NVT simulations facilitate diffusion coefficient calculations. In order to evaluate mechanical properties of the lithiated sulfur compositions, deformation simulations were carried out using the NPT ensemble in LAMMPS[66] at 300K and atmospheric pressure. The Nosé-Hoover thermostat and barostat[67] were used with temperature and pressure damping constants of 50fs and 1000fs, respectively. Periodic boundary conditions were employed in all three directions, and a MD time step of 0.25 fs was used for all the simulations in this study.

5. Force Field Validation

5.1 Phase diagram

To verify the quality of our Li-S potential in describing the various Li_xS phases, the Genetic Algorithm for Structure and Phase Prediction (GASP)[68,69] was employed. We used it to investigate the energy landscape of our potential, to identify low-energy configurations, and thus to construct the Li-S binary phase diagram, according to the potential. A GA is a heuristic optimization algorithm modeled after the biological process of evolution, and its purpose here is to find the lowest-energy configurations at every composition between pure Li and pure S. The algorithm uses the information learned from the early guesses and makes better guesses to produce improved structures later on. The initial structures, known as parent generation, are generated randomly within some hard constraints: maximum and minimum lattice parameters and number of atoms, interatomic distances, and number of species. New structures are evaluated by their formation energies with respect to the currently-known ground state phases. The lower this metric, the more likely a structure is to be chosen as a parent and used to generate offspring by means of mutation and mating operations. The algorithm proceeds by producing successive generations, and as it does, low energy structural motifs are likely to survive, while structures with high energy become less common.

The algorithm was run for 50 generations with 50 structures per generation, and the resulting Li-S phase diagram is shown in Figure 2. This diagram is constructed by plotting each structure encountered by the algorithm according to its formation energies with respect to the elements versus its composition. The lower convex bound on the points is known as convex hull and is used to determine the thermodynamic ground states and energies of the various Li-S compositions. The structures which lie on the convex hull are ground states at their composition. At compositions which have no

representative on the curve, the lowest-energy configuration is actually a mixture of materials at other compositions.
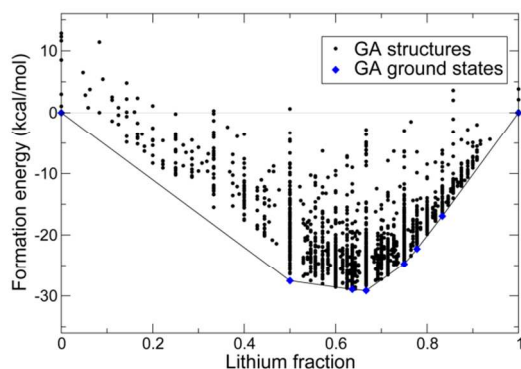

Figure 2. Convex hull phase diagram of Li$_x$S compositions.

For any structure, the vertical distance between its point and the convex hull is the energy difference between this phase and corresponding thermodynamic ground state. In the phase diagram, we identify stable binary structures with compositions LiS, Li$_7$S$_4$, Li$_2$S, Li$_3$S, Li$_7$S$_2$, and Li$_5$S, although all but LiS are barely stable with respect to Li$_2$S and the elements and are artifacts of the fitting procedure. The experimentally known binary phase, with composition Li$_2$S, is not the ground state according to the potential but lies only 0.24 kcal/mol above the convex hull.

5.2 Discharge voltage profile

We used the hybrid grand canonical Monte Carlo/molecular dynamics (GC-MC/MD) method described by Senftle *et al.*[70,71] to investigate lithium insertion into α-sulfur. We calculated heats of formation of lithiated sulfur compounds and found the corresponding open circuit voltage profile. A TP$_{\mu Li}$N$_S$ ensemble (constant pressure and adjustable volume) was used so that the structure could change its volume upon lithiation. The acceptance criterion used for lithium insertion into α-sulfur in this simulation is analogous to that described in Ref. [70]. Each MC trial move was followed by a low temperature MD based energy minimization to allow structural relaxation. This increases the MC acceptance rate by placing Li atoms into low energy sites.
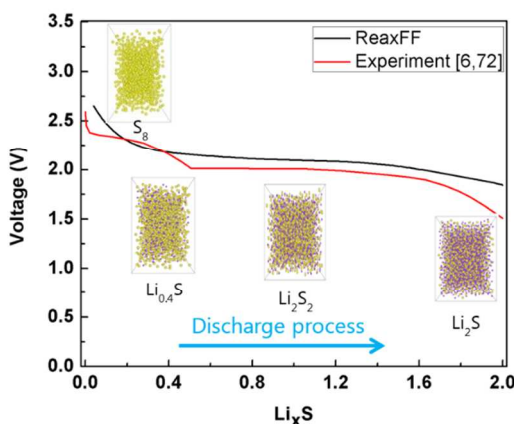

Figure 3. Open circuit voltage profile during lithiation of sulfur cathode. Yellow and purple represent sulfur and lithium atom respectively.

Heats of formation of the lithiated sulfur configurations as a function of lithium content with respect to α-sulfur and bcc-Li were calculated using the relation mentioned in the force field development section. Next, we calculated the open circuit voltage profile during lithiation as a function of lithium concentration. The voltage profile relative to Li/Li$^+$ is given by

$$V(x) = -\frac{G_{Li_xS} - xG_{Li} - G_S}{x}$$

where, G is the Gibbs free energy and x refers to the lithium concentration. Approximating enthalpic (PV) and entropic (TS) contributions are negligible; Gibbs free energy can be replaced by the ground state energy.

Discharge voltage profile corresponding to the reduction pathway of S$_8$ to Li$_2$S was calculated and is shown in Figure 3. The derived voltage profile is consistent with the results reported in Ref. [6,72] Likewise, the experimental observation, ReaxFF calculations nicely predict the initial drop in the voltage profile due to the formation of high molecular weight polysulfides and the flatter region and subsequent drop in the voltage approaching Li$_2$S.

5.3 Volumetric expansion of Li$_x$S compounds

The sulfur cathode undergoes significant volumetric expansion upon Li uptake. In this study, the volumes of a-Li$_x$S at various compositions were obtained from NPT simulations at 300 K and atmospheric pressure. The relative volume is plotted against lithium concentration in sulfur phase as shown in Figure 4.
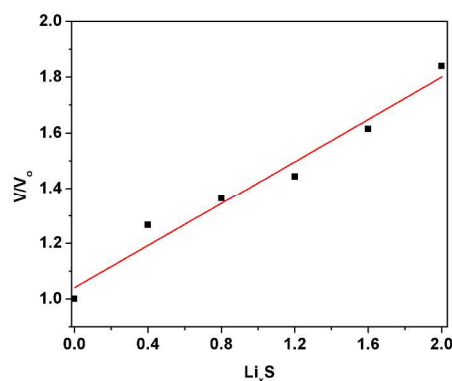

Figure 4. Volume expansion as a function of lithiation. V is the volume of the lithiated configurations and V$_o$ is the volume of unlithiated sulfur.

The volume of Li-S amorphous phases increases almost linearly with x. In the case of Li$_2$S, ReaxFF predicts a volume expansion of 83%, which is in excellent agreement with the reported experimental prediction of 80%.[14,24,73]

6. Results and Discussions

6.1 Structural properties

To evaluate the structural properties of lithiated sulfur compounds, we calculate radial distribution functions (RDF), g(r), and the number of atoms within first coordination shell using following formulae

$$g(r) = \frac{n(r)}{\rho \, 4\pi r^2 \Delta r} \qquad CN = \int_0^{r'} \rho . 4\pi \, r^2 . g(r) \, dr$$

where n(r) is the number of atoms within a distance r of a central atom, ρ is the bulk number density, r' is the distance to the first minima of g(r) from each atom, and CN is the coordination number. The RDFs are obtained by extracting trajectories at 0.125 pico second intervals from the 300K NVT simulations. S-S, Li-Li, and Li-S RDFs for all the a-Li$_x$S cases considered in this study are presented in Figure 5a-c.
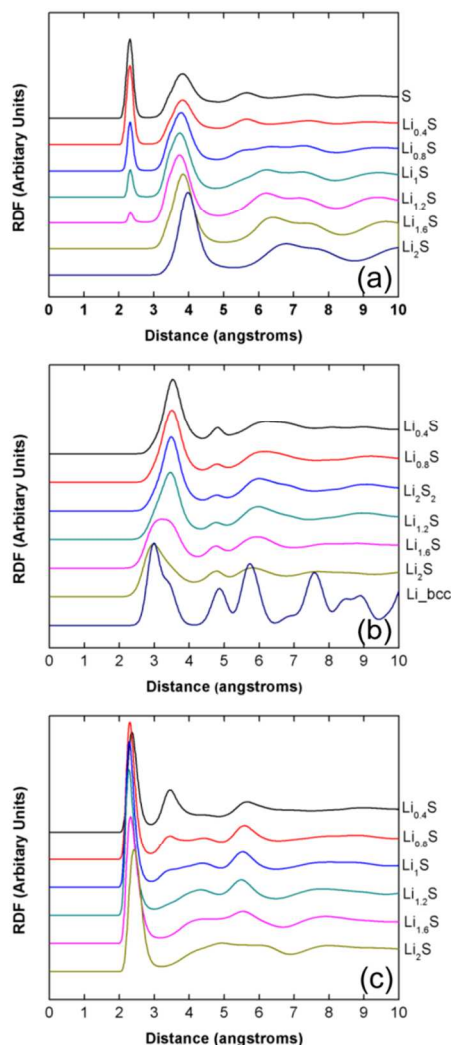

Figure 5. Radial distribution functions (a) S-S (b) Li-Li, and (c) S-Li atom pairs

In these RDFs, we observe peaks that are much broader than for typical crystalline materials. Along with the absence of sharp peaks at long-range, this suggests structural amorphization. In Figure 5a, with the increasing lithium content, the S-S first peak decreases, and the second peak increases. The first peak is attributed to the S-S covalent bond, while the second one around 4.0 Å corresponds to sulfur being bound through Li$^+$. Note that position of the second peak is slightly lower than double of the Li-S first peak. During lithiation the fraction of polysulfides (Li$_m$S$_n$, n≥2) decreases and fraction of Li$_x$S increases as indicated by diminishing magnitude of

the first peak of S-S RDF. At high lithium content sulfur is increasingly held together via lithium linkages as indicated by the increasing second peak located around 4.0 Å. Similarly, the Li-Li RDFs in Figure 5b show that at higher lithium concentrations, Li-Li interactions become stronger as bond lengths contract from 3.5Å to 3.0Å due to the formation of more Li$^+$-Li$^+$ bonding in Li$_x$S. The Li-Li RDFs for our model amorphous phases are also compared with the crystalline bcc-Li. The crystal's RDF indicates long range order and the calculated Li-Li bond length is also in conformity with reported value of 3.03Å.[74] In all the lithiated sulfur compounds, the nearest neighbor peak of Li-S atom pairs remain close to 2.2Å to 2.3Å as shown in Figure 5c.

6.2 Mechanical properties

To characterize the mechanical behavior of the a-Li$_x$S compounds, we performed room temperature MD simulations and obtained the stress-strain relationship under uniaxial tensile loading. We considered five different uniaxial strain rates (1x10^8, 5x10^8, 1x10^9, 1x10^{10}, 1x10^{11} s^{-1}) to investigate the effect of strain rate on the mechanical properties. Stresses are calculated based on the definition of virial stress, which is expressed as

$$\sigma_{virial}(r) = \frac{1}{\Omega} \sum_i \left[\left(-m_i \dot{u}_i \otimes \dot{u}_i + \frac{1}{2} \sum_{j \neq i} r_{ij} \otimes f_{ij} \right) \right]$$

where the summation is over all the atoms occupying the total volume, m_i is the mass of atom i, is the time derivative which indicates the displacement of atom with respect to a reference position, , where is the position vector of atom , is the cross product, and is the interatomic force applied on atom i by atom j.

Figure 6a-c shows tensile stress-strain curves at three strain rates for all the lithiated sulfur cases considered in this work. Stress-strain curves for the strain rate of 5 x10^8 and 1x10^8 (s^{-1}) are provided in the Figure S1 of the supplementary information. At lower strain rates, past the elastic limit, stress rises and drops repeatedly with the strain, while under faster loading, no such fluctuations are observed. Similar trends in the stress-strain curve at other strain rates have been observed in amorphous Ni-nanowire deformation simulations.[75] The zigzag stress-strain curve after the elastic limit at lower strain rate and higher lithiation cases are due to the stress-relaxation during tensile loading. At a strain rate of 10^{11} s^{-1}, the maximum stress occurs at ~15% strain. However, at a lower strain rate, it shifts to ~10% strain. In general, stress-strain curves exhibit an initial linear region followed by a nonlinear portion and then a drop in stress. The linear portion of the uniaxial stress-strain curve corresponds to elastic deformation and the gradient of this part is Young's modulus (YM). In this study, YM was calculated using linear regression on the initial linear portion. The yield strength was computed by plotting a line parallel to the linear part of the stress-strain curve at 0.2 percent strain offset. The intersection between this 0.2 percent offset line and stress-strain curve gives the yield strength. The ultimate strength is the maximum stress experienced during tensile loading. Effect of strain-rate on various mechanical properties and the lithiation-induced variation in strength for the a-Li$_x$S cases are presented in Figure 6d-f. We see that the strain-rate has significant consequences for all the material properties. During tensile loading, the combination of both elastic and anelastic (time-dependent, fully reversible deformation) strains determine the mechanical behavior of the materials.
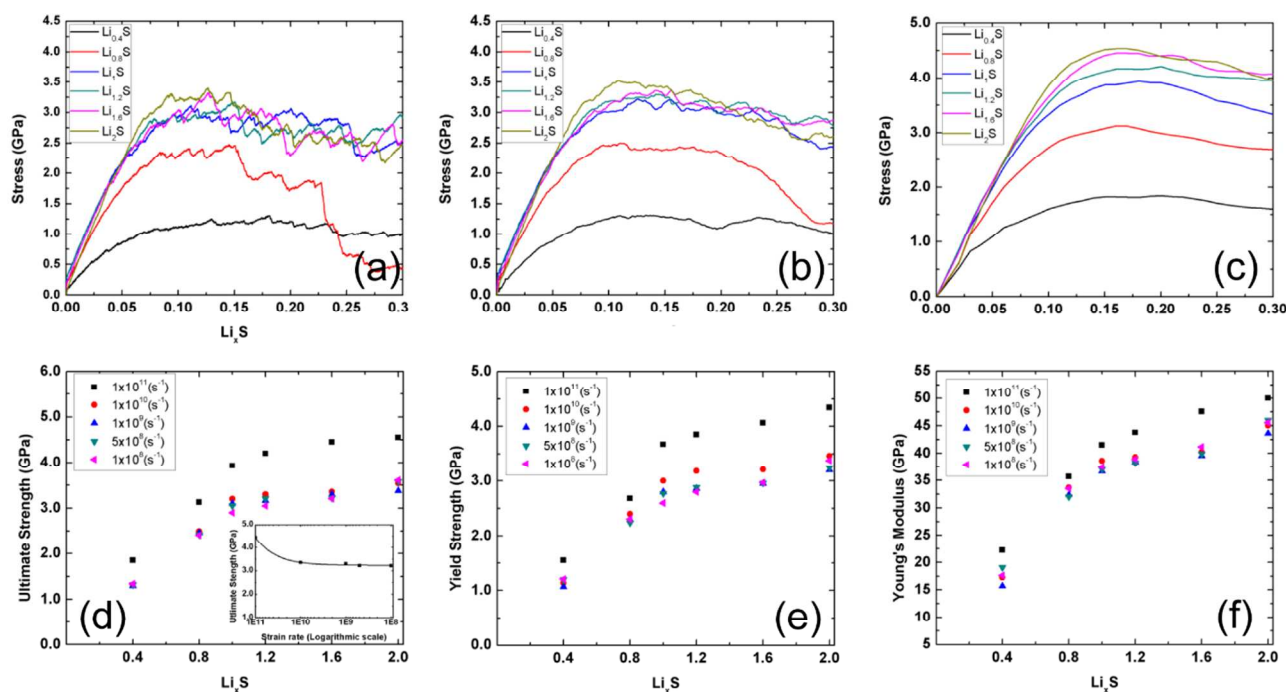
Figure 6. Stress-strain curve for the a-Li_xS compositions at different strain rate (a) 1×10^9 s^{-1} (b) 1×10^{10} s^{-1}, and (c) 1×10^{11} s^{-1}; other mechanical properties (d) Ultimate strength (e) Yield strength, and (f) Young's modulus; inset of (d) shows the convergence in the ultimate strength with the strain rate for the case of $Li_{1.6}S$.

At higher loading rates, anelastic strain approaches zero resulting in entirely elastic strain, while at low-strain-rates both of them accompany the loading process that contributes to the lower strength.[76] Moreover, increases in strain rate enhance the flow stress that directly influences the mechanical behavior. The calculated Young's modulus, ultimate strength, and yield strength at low-strain-rate are lower than that at high-strain-rates. This trend is consistent with the experimental observations for amorphous materials.[77] It can be seen from Figure 6d-f that strain rate converges at 1×10^{10} s^{-1} and the reported strength and YM values are in close proximity for the strain rate of 1×10^{10}(s^{-1}) and lower. The calculated YM value for Li_2S is ~45GPa, which is lower than the previously reported[78] DFT-GGA results of 76.6 GPa, the discrepancy is likely due to the absence of thermal effects in DFT optimization. However, extrapolation of the Young modulus of the dense hot pressed Li_2S-P_2S_5 pellets to 100% Li_2S composition would yield values around 35GPa, which is in excellent agreement with the ReaxFF predictions.[79]

It is evident that lithiated sulfur compounds undergo strain hardening with increasing lithium concentration. Lithiation also augments toughness and ductility of the lithiated compounds. Toughness is the amount of energy absorbed by a material before its failure. We observe that improvement in material strength is rapid during initial lithiation, but beyond $Li_{1.2}S$ strengthening is not substantial. During initial lithium loading, Li-S bonds are formed through the cleavage of S-S bonds. This contributes to the increase in strength, while at higher lithium content, Li-Li bond formation contributes to the strength increment to a lesser extent. Interestingly, the lithiation induced mechanical response of the a-Li_xS compounds is quite opposite of that observed for the a-Li_xSi alloys. Lithiation degrades the mechanical properties of silicon,[10,80] while in case of sulfur, it enhances the strength of the material. Lithiation of Si causes breaking of Si-Si bonds and subsequent formation of the Li-Si

bonds. The softening effect due to the lithium insertion into the Si is attributed to the decrease in the number of strong covalent Si-Si bonds as they breaks and replaced by the weaker ionic Li-Si bonds. Shenoy et al.[81] reported the elastic moduli of the amorphous-Si and Li are 92 and 20 GPa, respectively. Our ReaxFF calculations predict the elastic moduli of Li and S as 23 and 5.78 GPa, respectively. Therefore, insertion of the Li into the softer S resulting in the increase of the strength of Li_xS compositions.

In addition, we studied the failure behavior of lithiated sulfur compositions during tensile loading. Fracture initiates via the formation of small voids in the structure, followed by the coalescence of multiple voids that leads to necking. As the tensile loading continues, stress concentration at the necking region eventually leading to rupture. This failure mode is commonly observed in amorphous materials. An example of failure behavior for $Li_{0.8}S$ is shown in Figure 7.
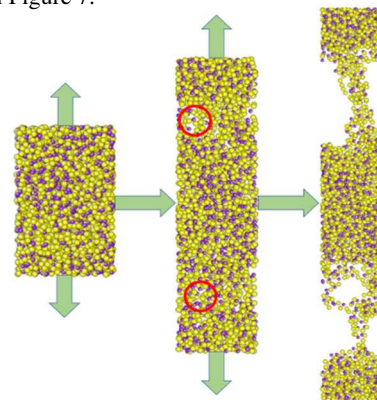

Figure 7. Failure behavior of $Li_{0.8}S$ composition upon tensile loading. Fracture initiates via formation of voids. Yellow and purple represent sulfur and lithium atom, respectively.

6.3 Diffusion coefficients

For the analysis of the diffusion of lithium and sulfur in a-Li_xS, we carried out NVT MD simulations at several temperatures. We stored unfolded trajectories generated from the NVT MD simulations at every 0.125 ps and calculated the mean-square displacement (MSD) as a function of the position of each diffusing particle. MSDs and diffusion coefficients (DCs) were calculated using Einstein's relation

$$MSD = < |r(t) - r(0)|^2 >$$

$$D = \frac{1}{6} \lim_{\Delta t \to \infty} \frac{MSD(t + \Delta t) - MSD(t)}{\Delta t}$$

where r is the position of the particle, t is the time, and D is the diffusion coefficient.

Because of the slow rate of diffusion of both species in the Li_xS compositions, it was challenging to calculate DCs at 300K given our MD time scale. Therefore, we calculated DC at elevated temperatures using the above equations. To facilitate DC calculation at room temperature, we extrapolated our elevated temperature data through the following Arrhenius equation[82]

$$D(T) = D_o \exp(-\frac{E_a}{kT})$$

where D_0 is the pre-exponential factor, E_a is the activation energy, k is the Boltzmann constant, and T is the temperature. The activation energy and pre-exponential factors are independent of temperature and were computed using an exponential regression analysis of a D vs. 1/T plot.
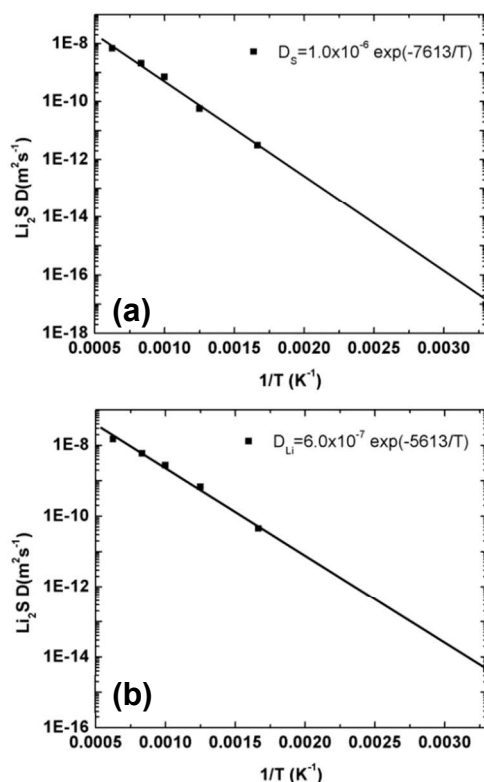

Figure 8. Arrhenius plot for calculating diffusion coefficient at 300K, (a) sulfur, and (b) lithium

Figure 8 shows the relationship between diffusivity and temperature through the Arrhenius equation for the sulfur and lithium in the Li_2S case. Using the Arrhenius plot, we calculated 300K diffusion coefficients for both Li and S via extrapolation of our high temperature data. This is presented in Figure 9. It is evident that diffusivity of both species depends strongly on the lithium concentration. Interestingly, lithium and sulfur DCs decrease initially with the lithiation, but this trend soon reverses. We observe that DCs of both species are of the same order of magnitude up to $Li_{1.2}S$.

However, further lithiation increases Li diffusivity to two orders of magnitude higher than that of S, which indicates that at higher lithium concentration, Li is the dominating diffusion species. The difference in DC between these two species at higher lithium concentration may be responsible for stress generation where lithium atoms have to push sulfur in order to diffuse in the cathode material. On the other hand, at lower lithium concentrations, lithium diffuses as fast as sulfur, minimizing diffusion induced stress.
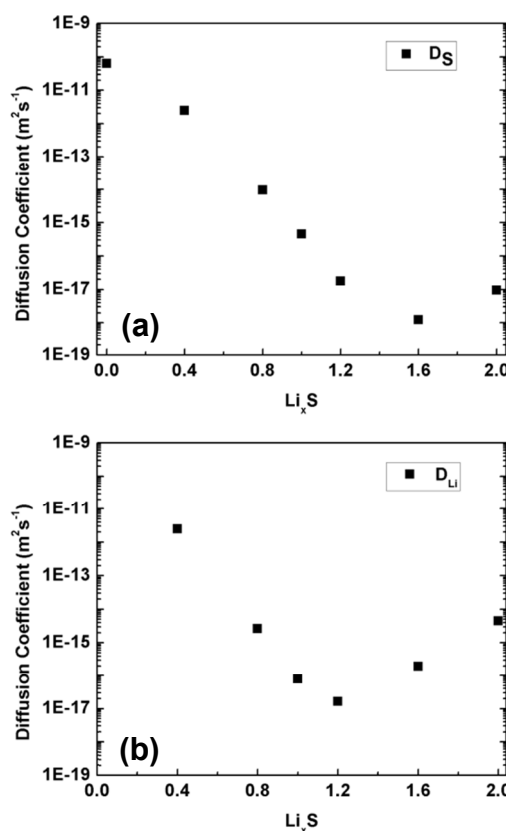

Figure 9. Diffusion coefficient of (a) sulfur, and (b) lithium at 300K, calculated using Arrhenius relation.

Our calculated range of the lithium DCs is comparable with the typical range of lithium diffusivity in the conventional transition metal oxide/phosphate cathodes.[83,84] However, given that the insulating characteristics of Li_xS compositions, apparently, our extrapolated data is the upper bound to the Li and S diffusion coefficients. The diffusivity of lithium or sulfur in the Li_xS compounds exhibits an opposing behavior that of the a-Li_xSi alloys. Lithiation in Si increases lithium and silicon diffusivity initially.

However, with further lithiation, the diffusivity of both species dwindles.[9]

7. Conclusions

We developed a ReaxFF potential for describing Li-S interactions and performed MD simulations to study various structural, mechanical, and diffusion properties in a-Li$_x$S compounds. ReaxFF reproduces the experimental open circuit voltage profile during cell discharge. The volume expansion of the a-LixS compositions captured in our simulations matches experimental observations well. The phase diagram produced by a GA search of the potential provides information about the formation energies of the various Li$_x$S phases as a function of composition. GA scheme exhibits that experimentally known Li$_2$S structure lies in a very close proximity of the convex hull, i.e. ground state. Our simulations for calculating mechanical properties of a-Li$_x$S illustrate that lithiated sulfur compounds undergo strain hardening with lithiation, which results in an increase in strength and toughness. Dependence of the mechanical properties of a-Li$_x$S compounds on strain rate is observed: the material exhibits higher strength with increasing strain rate. Young Modulus from our calculations was found in good agreement with the extrapolated experimental values. Diffusion coefficients of both lithium and sulfur are contingent on the lithium content in a-Li$_x$S compositions. These demonstrate that the developed Li-S potential can accurately describe Li-S chemistry.

This newly developed Li-S potential and its application to lithiated sulfur systems provides a new perspective on lithiation induced mechanical responses of sulfur cathodes at the most fundamental atomistic level. The computed material properties will enable the development of a continuum model to further investigate the morphological evolution, degradation, and failure mechanism of lithiated sulfur during electrochemical cycling for specimens of experimental length and time scale. We believe these atomistic-level insights will play a vital role in designing cathode materials for high performance Li-S batteries to meet future energy demand.

Acknowledgments

Notes and References

[a]Department of Mechanical and Nuclear Engineering, The Pennsylvania State University, University Park, PA 16802, USA
[b]Department of Engineering Science and Mechanics, The Pennsylvania State University, University Park, PA 16802, USA
[c]Electrochemistry Branch, US Army Research Laboratory, 2800 Powder Mill Rd., Adelphi, MD 20783, USA
[d]Materials and Manufacturing Directorate, Air Force Research Laboratory, AFRL/RXBN, Wright-Patterson AFB, OH 45433-7750, USA
[e]Department of Materials Science and Engineering, Cornell University, Ithaca, NY 14853, USA
[f]Sandia National Laboratories, Albuquerque, New Mexico 87185, USA
[a]*Email: *acv13@psu.edu*, Phone: (814) 863-6277, Fax: (814) 863-6382

†*Electronic supplementary information (ESI) available.See DOI:*

1   J.-M. Tarascon and M. Armand, *Nature*, 2001, **414**, 359–367.
2   M. S. Whittingham, *Chem. Rev.*, 2004, **104**, 4271–4302.
3   M. Nagao, Y. Imade, H. Narisawa, T. Kobayashi, R. Watanabe, T. Yokoi, T. Tatsumi and R. Kanno, *J. Power Sources*, 2013, **222**, 237–242.
4   M.-K. Song, S. Park, F. M. Alamgir, J. Cho and M. Liu, *Mater. Sci. Eng. R Rep.*, 2011, **72**, 203–252.
5   M.-K. Song, E. J. Cairns and Y. Zhang, *Nanoscale*, 2013, **5**, 2186–2204.
6   X. Ji, K. T. Lee and L. F. Nazar, *Nat. Mater.*, 2009, **8**, 500–506.
7   J. Shim, K. A. Striebel and E. J. Cairns, *J. Electrochem. Soc.*, 2002, **149**, A1321–A1325.
8   M. K. Y. Chan, C. Wolverton and J. P. Greeley, *J. Am. Chem. Soc.*, 2012, **134**, 14362–14374.
9   Z. Cui, F. Gao, Z. Cui and J. Qu, *J. Power Sources*, 2012, **207**, 150–159.
10   K. Zhao, G. Tritsaris, M. Pharr, W. Wang, O. Okeke, Z. Suo, J. Vlassak and E. Kaxiras, *NanoLetters*, 2012, **12**, 4397–4403.
11   B. Scrosati and J. Garche, *J. Power Sources*, 2010, **195**, 2419–2430.
12   F. Fan, S. Huang, H. Yang, M. Raju, D. Datta, V. B. Shenoy, A. C. T. van Duin, S. Zhang and T. Zhu, *Model. Simul. Mater. Sci. Eng.*, 2013, **21**, 074002.
13   C.-Y. Chou, H. Kim and G. S. Hwang, *J. Phys. Chem. C*, 2011, **115**, 20018–20026.
14   G. Zheng, Y. Yang, J. J. Cha, S. S. Hong and Y. Cui, *Nano Lett.*, 2011, **11**, 4462–4467.
15   L. Ji, M. Rao, H. Zheng, L. Zhang, Y. Li, W. Duan, J. Guo, E. J. Cairns and Y. Zhang, *J. Am. Chem. Soc.*, 2011, **133**, 18522–18525.
16   Y. Yang, M. T. McDowell, A. Jackson, J. J. Cha, S. S. Hong and Y. Cui, *Nano Lett.*, 2010, **10**, 1486–1491.
17   S. S. Zhang, *J. Power Sources*, 2013, **231**, 153–162.
18   L. Chen and L. L. Shaw, *J. Power Sources*, 2014, **267**, 770–783.
19   X. He, J. Ren, L. Wang, W. Pu, C. Jiang and C. Wan, *J. Power Sources*, 2009, **190**, 154–156.
20   Y.-X. Yin, S. Xin, Y.-G. Guo and L.-J. Wan, *Angew. Chem. Int. Ed.*, 2013, n/a–n/a.
21   L. Yuan, H. Yuan, X. Qiu, L. Chen and W. Zhu, *J. Power Sources*, 2009, **189**, 1141–1146.
22   F. Wu, A. Magasinski and G. Yushin, *J. Mater. Chem. A*, 2014, **2**, 6064–6070.
23   H. Wang, Y. Yang, Y. Liang, J. T. Robinson, Y. Li, A. Jackson, Y. Cui and H. Dai, *Nano Lett.*, 2011, **11**, 2644–2647.
24   F. Zhang, X. Zhang, Y. Dong and L. Wang, *J Mater Chem*, 2012, **22**, 11452–11454.
25   M. Barghamadi, A. Kapoor and C. Wen, *J. Electrochem. Soc.*, 2013, **160**, A1256–A1263.
26   J. Kim, D.-J. Lee, H.-G. Jung, Y.-K. Sun, J. Hassoun and B. Scrosati, *Adv. Funct. Mater.*, 2013, **23**, 1076–1080.
27   D.-R. Chang, S.-H. Lee, S.-W. Kim and H.-T. Kim, *J. Power Sources*, 2002, **112**, 452–460.
28   J. Hassoun, J. Kim, D.-J. Lee, H.-G. Jung, S.-M. Lee, Y.-K. Sun and B. Scrosati, *J. Power Sources*, 2012, **202**, 308–313.
29   H. Wang, W.-D. Zhang, Z.-Q. Deng and M.-C. Chen, *Solid State Ion.*, 2009, **180**, 212–215.
30   T. Osaka, T. Momma, Y. Matsumoto and Y. Uchida, *J. Electrochem. Soc.*, 1997, **144**, 1709–1713.
31   N. J. Dudney, *J. Power Sources*, 2000, **89**, 176–179.
32   X. Liang, Z. Wen, Y. Liu, M. Wu, J. Jin, H. Zhang and X. Wu, *J. Power Sources*, 2011, **196**, 9839–9843.
33   K. Nishikawa, Y. Fukunaka, T. Sakka, Y. H. Ogata and J. R. Selman, *J. Electrochem. Soc.*, 2007, **154**, A943–A948.
34   N. Liu, L. Hu, M. T. McDowell, A. Jackson and Y. Cui, *ACS Nano*, 2011, **5**, 6487–6493.
35   Y. Yang, G. Zheng, S. Misra, J. Nelson, M. F. Toney and Y. Cui, *J. Am. Chem. Soc.*, 2012, **134**, 15387–15394.
36   K. Cai, M.-K. Song, E. J. Cairns and Y. Zhang, *Nano Lett.*, 2012, **12**, 6474–6479.
37   X. He, J. Ren, L. Wang, W. Pu, C. Wan and C. Jiang, *Ionics*, 2009, **15**, 477–481.
38   C. R. Jarvis, M. J. Lain, M. V. Yakovleva and Y. Gao, *J. Power Sources*, 2006, **162**, 800–802.
39   M. M. Islam, V. S. Bryantsev and A. C. T. van Duin, *J. Electrochem. Soc.*, 2014, **161**, E3009–E3014.
40   J. Tersoff, *Phys. Rev. Lett.*, 1988, **61**, 2879–2882.
41   D. W. Brenner, *Phys. Rev. B*, 1990, **42**, 9458–9471.

ARTICLE

Physical Chemistry Chemical Physics Accepted Manuscript

42 T. Liang, Y. K. Shin, Y.-T. Cheng, D. E. Yilmaz, K. G. Vishnu, O. Verners, C. Zou, S. R. Phillpot, S. B. Sinnott and A. C. T. van Duin, *Annu. Rev. Mater. Res.*, 2013, **43**, 109–129.

43 A. C. Van Duin, A. Strachan, S. Stewman, Q. Zhang, X. Xu and W. A. Goddard, *J. Phys. Chem. A*, 2003, **107**, 3803–3811.

44 K. D. Nielson, A. C. van Duin, J. Oxgaard, W.-Q. Deng and W. A. Goddard, *J. Phys. Chem. A*, 2005, **109**, 493–499.

45 W. J. Mortier, S. K. Ghosh and S. Shankar, *J. Am. Chem. Soc.*, 1986, **108**, 4315–4320.

46 A. C. Van Duin, S. Dasgupta, F. Lorant and W. A. Goddard, *J. Phys. Chem. A*, 2001, **105**, 9396–9409.

47 K. Chenoweth, A. C. T. van Duin and W. A. Goddard, *J. Phys. Chem. A*, 2008, **112**, 1040–1053.

48 M. F. Russo Jr. and A. C. T. van Duin, *Nucl. Instrum. Methods Phys. Res. Sect. B Beam Interact. Mater. At.*, 2011, **269**, 1549–1554.

49 D. Bedrov, G. D. Smith and A. C. van Duin, *J. Phys. Chem. A*, 2012, **116**, 2978–2985.

50 F. Castro-Marcano, A. M. Kamat, M. F. Russo Jr, A. C. van Duin and J. P. Mathews, *Combust. Flame*, 2012, **159**, 1272–1285.

51 A. C. T. van Duin, J. M. A. Baas and B. van de Graaf, *J. Chem. Soc. Faraday Trans.*, 1994, **90**, 2881.

52 M. W. Schmidt, K. K. Baldridge, J. A. Boatz, S. T. Elbert, M. S. Gordon, J. H. Jensen, S. Koseki, N. Matsunaga, K. A. Nguyen, S. Su and others, *J. Comput. Chem.*, 1993, **14**, 1347–1363.

53 M. Head-Gordon, J. A. Pople and M. J. Frisch, *Chem. Phys. Lett.*, 1988, **153**, 503–506.

54 A. I. Boldyrev, J. Simons and P. von R. Schleyer, *J. Chem. Phys.*, 1993, **99**, 8793.

55 M. W. Wong, Y. Steudel and R. Steudel, *Chem. Phys. Lett.*, 2002, **364**, 387–392.

56 P. Hohenberg and W. Kohn, *Phys. Rev.*, 1964, **136**, B864.

57 W. Kohn and L. J. Sham, *Phys. Rev.*, 1965, **140**, A1133.

58 G. Kresse and J. Hafner, *Phys. Rev. B*, 1993, **48**, 13115.

59 G. Kresse and J. Furthmüller, *Phys. Rev. B*, 1996, **54**, 11169.

60 P. E. Blöchl, *Phys. Rev. B*, 1994, **50**, 17953.

61 J. P. Perdew, K. Burke and M. Ernzerhof, *Phys. Rev. Lett.*, 1996, **77**, 3865–3868.

62 E. Zintl, A. Harder and B. Dauth, *Z Elektrochem Angew Phys Chem*, 1934, **40**, 588–593.

63 R. S. Assary, L. A. Curtiss and J. S. Moore, *J. Phys. Chem. C*, 2014.

64 L. A. Curtiss, P. C. Redfern and K. Raghavachari, *J. Chem. Phys.*, 2007, **126**, 084108.

65 H. J. C. Berendsen, J. P. M. Postma, W. F. van Gunsteren, A. DiNola and J. R. Haak, *J. Chem. Phys.*, 1984, **81**, 3684–3690.

66 S. Plimpton, *J. Comput. Phys.*, 1995, **117**, 1–19.

67 W. G. Hoover, *Phys. Rev. A*, 1985, **31**, 1695.

68 W. W. Tipton, C. R. Bealing, K. Mathew and R. G. Hennig, *Phys. Rev. B*, 2013, **87**, 184114.

69 W. W. Tipton and R. G. Hennig, *J. Phys. Condens. Matter*, 2013, **25**, 495401.

70 T. P. Senftle, M. J. Janik and A. C. T. van Duin, *J. Phys. Chem. C*, 2014.

71 T. P. Senftle, R. J. Meyer, M. J. Janik and A. C. T. van Duin, *J. Chem. Phys.*, 2013, **139**, 044109.

72 P. G. Bruce, S. A. Freunberger, L. J. Hardwick and J.-M. Tarascon, *Nat. Mater.*, 2012, **11**, 19–29.

73 H. Chen, W. Dong, J. Ge, C. Wang, X. Wu, W. Lu and L. Chen, *Sci. Rep.*, 2013, **3**.

74 L. E. Sutton, *Tables of Interatomic Distances and Configuration in Molecules and Ions: Supplement 1956-59*, Chemical Society, 1965.

75 P. S. Branício and J.-P. Rino, *Phys. Rev. B*, 2000, **62**, 16950.

76 J. R. Davis, *Tensile Testing*, ASM International, 2004.

77 M. L. Falk and J. S. Langer, *ArXiv Prepr. ArXiv10044684*, 2010.

78 H. Khachai, R. Khenata, A. Bouhemadou, A. H. Reshak, A. Haddou, M. Rabah and B. Soudini, *Solid State Commun.*, 2008, **147**, 178–182.

79 A. Sakuda, A. Hayashi and M. Tatsumisago, *Sci. Rep.*, 2013, **3**.

80 K. Zhao, W. L. Wang, J. Gregoire, M. Pharr, Z. Suo, J. J. Vlassak and E. Kaxiras, *Nano Lett.*, 2011, **11**, 2962–2967.

81 V. B. Shenoy, P. Johari and Y. Qi, *J. Power Sources*, 2010, **195**, 6825–6830.

82 A. C. van Duin, B. V. Merinov, S. S. Han, C. O. Dorso and W. A. Goddard Iii, *J. Phys. Chem. A*, 2008, **112**, 11414–11422.

83 S. Franger, F. L. Cras, C. Bourbon and H. Rouault, *Electrochem. Solid-State Lett.*, 2002, **5**, A231–A233.

84 L.-X. Yuan, Z.-H. Wang, W.-X. Zhang, X.-L. Hu, J.-T. Chen, Y.-H. Huang and J. B. Goodenough, *Energy Environ. Sci.*, 2011, **4**, 269–284.